

Experimental Study of VHCF Fractographic Features of Conventionally and Additively Manufactured Steels

M. F. Andrade^{a*} , M. C. Teixeira^a , M. V. Pereira^a 

^aPontifícia Universidade Católica do Rio de Janeiro, Departamento de Engenharia Química e de Materiais, Rua Marquês de São Vicente, 225, 22453-900, Rio de Janeiro, RJ, Brasil.

Received: June 08, 2022; Revised: January 18, 2023; Accepted: February 01, 2023

Materials produced by additive manufacturing (AM) have been extremely related to literature. However, there is still unconsolidated knowledge about the fatigue life and respective mechanisms of initiation of cracks predominant in the VHCF regime for these materials. What has been observed in materials produced by conventional routes is that fatigue cracks tend to nucleate from intrinsic defects of the material located internally or in subsurface regions. The change in the evolution process of fatigue cracks leads to the formation of a characteristic morphology on the fracture surface, known as “fish-eye”. Another widespread aspect observed on the fracture surfaces is the formation of a fine granular area (FGA) nearby the initiation sites. This work aims to investigate the mechanisms of crack nucleation in VHCF of two distinct materials: conventional steel, DIN 34CrNiMo6 and AISI 316L stainless steel produced by L-DED. The ultrasonic tests were carried out at a frequency of $20 \pm 0,5$ kHz and $R = -1$. The S-N curves were obtained and fracture surfaces were analyzed, fish-eye and FGA formation was verified. FGA sizes were compared to values estimated by empirical equations. FGA and fish-eye sizes were related to stress amplitude and maximum stress intensity factor (SIF).

Keywords: *Ultrasonic fatigue, FGA size, fish-eye, additive manufacturing (AM).*

1. Introduction

Very high cycle fatigue (VHCF) has assumed a relevant role in recent years. Due to technological development, the fatigue life of structural and mechanical components usually exceeds the high cycle regime ($10^6 - 10^7$ cycles)¹.

Recently, a growing study of additive manufacturing (AM) applied to ultrasonic fatigue tests has been observed. AM is becoming a promising technique for a number of applications in aerospace, automotive and medical industries. This technique is used to repair high-value-added components or manufacture new 3D parts. The process offers great flexibility in terms of the feed material (metallic powder or filler wire), it also allows the manufacture of multifunctional 3D components from different materials simultaneously²⁻⁶. Several materials can be used in this process, but AISI 316L stainless steel is one of the most studied and processed by these techniques due to the excellent properties (weldability, corrosion resistance and tensile properties) that are preserved in the final parts⁶.

The AM process, as L-DED (direct energy deposition by laser), is reported in the literature as an extremely sensitive technique to process parameters¹⁻⁶. Typical defects produced by AM processes are pores, voids, metallic inclusions, lack of fusion, among others⁶. It has been reported by several authors that all the mentioned defects favor crack initiation in the VHCF regime⁶⁻¹².

Phenomena belonging to the VHCF regime, such as “fish-eye” and fine granular area (FGA) are commonly

observed on the specimens' fracture surface, mainly high-strength steel manufactured by conventional routes⁶⁻¹² (the expression means - conventional steel manufacturing and casting process with subsequent forging and quenching and tempering treatment). However, there is still no consolidated knowledge about these features in AM materials.

This study compares the fracture surfaces of the specimens that present subsurface or internal crack nucleation after VHCF tests. The proposed steels were manufactured by conventional route (DIN 34CrNiMo6) and additively (AISI 316L). The main aims of this study were to measure the fish-eye and FGA regions and compare them with the values obtained by empirical equations available in the literature.

1.1. Fracture surface aspects

The fracture surface in VHCF can present different characteristics in comparison to other regimes. Many researchers have observed internal or subsurface crack initiation usually at non-metallic inclusions, indicating that VHCF is more sensitive to internal defects⁷⁻¹². The fracture surface exhibits a circular fatigue crack propagation, called fish-eye and an FGA nearby the inclusion responsible for the nucleation of the crack. These phenomena occur mainly in high-strength steels and result in a fracture surface with four stages for crack formation, as presented in Figure 1: crack initiation (i), crack growth into the fish-eye (ii), crack growth outside the fish-eye (iii) and final fracture (iv)^{7,10,11}.

Figure 2 presents the crack stages and their aspects with a transverse sectional view. FGA (2) region is the appearance

*e-mail: matheus-fernandes-andrade@outlook.com

vicinity of the internal defects (1 – e.g. inclusion) and exhibits a rough surface. Sakai¹³ attributes its formation to a sequence of three stages: polygonization, nucleation and coalescence of micro debonding and complete formation of the FGA. The fish-eye region (3) presents a smooth surface and finally (4) representing the crack growth stage exhibits again a high roughness region. The figure on the right represents schematically the regions indicated in the figure on the left and their respective roughness.

1.2. FGA size equations

It is known that FGA is an important phenomenon on fracture surfaces in the VHCF regime. The stress intensity factor (SIF) value of the FGA boundary can be related to the threshold for short crack growth. The crucial role of the FGA in the VHCF regime led some authors to investigate the FGA formation mechanisms and FGA size. Empirical equations to estimate the FGA size (diameter) are available in the literature. Murakami^{14,15}, Liu et al.¹⁶ and Yang¹⁷ proposed that the FGA size increases with the decreasing the stress amplitude and its size is dependent on the mechanical properties of the material and the applied stress amplitude (σ_a). The following are the presented empirical equations (Equations 1-3) proposed by these authors.

Yang¹⁷ obtained an empirical equation in which FGA size by fracture mechanics. The FGA is dependent on the

material's yield strength (σ_y) and σ_a . The FGA size is given in meters and it is represented by ϕ_{FGA} ¹⁸⁻²⁰.

$$\phi_{FGA} = 1240 \frac{1}{\sigma_y} \frac{1}{\sigma_a^2} \quad (1)$$

An equation proposed by Murakami and co-authors^{14,15} indicates the FGA size is dependent on the Vickers hardness (HV) and σ_a and the crack initiation site. The constant (C) is modified according to the crack nucleation origin, being 1.43 for subsurface crack initiation and 1.56 for internal crack initiation¹⁸⁻²⁰.

$$\sqrt{area_{FGA}} = \left[\frac{C(HV + 120)}{\sigma_a} \right]^6 \quad (2)$$

Equation 3, as follows, is similar to Equation 2. Therefore, Liu and co-authors¹⁶ proposed a single value for C . In this way, the constant C becomes independent of the crack initiation site¹⁸⁻²⁰.

$$\sqrt{area_{FGA}} = \left[\frac{2(HV + 120)}{\sigma_a} \right]^6 \quad (3)$$

2. Materials

The materials used for this study was high-strength steel manufactured from a conventional route, DIN 34CrNiMo6²¹ and stainless steel by additive manufacturing, AISI 316L²². Table 1 shows the chemical composition with main elements and Table 2 presents the mechanical properties of both materials. The chemical characterization was performed with the Inductively Coupled Plasma Optical Emission Spectrometry (ICP-OES) technique and the tension tests were conducted in an Instron 5988 equipment according to ASTM A370²³. For the tension tests, a laser extensometer was applied to measure the deformation and the 0.2% offset method was used to calculate the elastic modulus and yield strength.

The AISI 316L stainless steel produced by additive manufacturing was produced using metallic powder by L-DED (direct energy deposition by laser) process in an RPM Innovations 535 machine with a 25° nozzle. The metallic powder used for the manufacture of all specimens was a gas atomized 316L stainless steel powder (code 316L-5520), made by Höganäs company. The powder particles are predominantly spherical, with a granulometric distribution of 53-150 μm ^{24,25}. The process parameters used in the manufacturing procedure were defined by prior empirical knowledge of the equipment and processing of this alloy²².

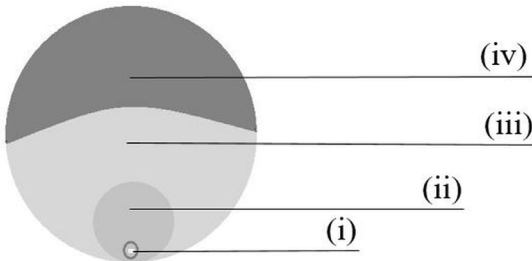
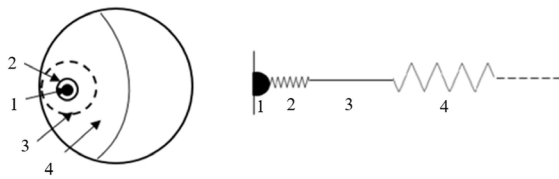


Figure 1. Crack growth stages in VHCF regime (adapted⁷).



1- Inclusion; 2 - FGA; 3 - Fish-eye; 4 - Crack growth.

Figure 2. Surface aspects of the crack stages (adapted¹³).

Table 1. Chemical composition restricted to main elements.

Steel	Fe (%)	C (%)	Cr (%)	Mo (%)	Ni (%)
DIN 34CrNiMo6	95.1	0.38	1.51	0.24	1.75
AISI 316L (AM)	68.5	0.02	16.9	2.5	12.7

Table 2. Mechanical properties with average/standard deviation.

Steel	σ_a (MPa)	σ_y (MPa)	E (GPa)	HV
DIN 34CrNiMo6	900/4.75	760/2.34	207/2.95	330/7.95
AISI 316L (AM)	575/1.25	298/0.82	203/32.27	195/11.1

All specimens were vertically built in the form of cylindrical bars using the same process parameters, which are indicated in Table 3. For each specimen, the outer boundary was primarily deposited and then the filling. For that, in each layer was used the zigzag deposition strategy and the direction of the filling passes was rotated 45° incrementally (0°, 45°, 90°, 135°, 180°, 225°, 270°, 315°, 0°).

After the fabrication process, the samples were subjected to heat treatments of stress relief followed by solubilization. In the stress relief treatment, the samples were kept at 550°C for 6 hours and cooled in air (cooling rate equal to 5° C/min). In the solubilization, they were kept at 1070°C for 2 hours, considering 1 hour for a soak and 1 hour for the treatment, and later they were cooled in two stages: initially in the saline solution until 260°C and soon after in air until the room temperature. The cooling rate in air was equivalent to 5° C/min and in the saline solution was equal to 100° C/min, respectively. And then, all the specimens for the VHCF test were machined.

3. Methodology

3.1. VHCF test

Both materials tests were performed in an ultrasonic fatigue machine (frequency = 20 kHz) with loading conditions $R=-1$ and controlled temperature. Figure 3 presents the schematic drawing of the displacement and stress distribution along the system with the main four components of the machine. In the absence of standardization, the ultrasonic test machines differ from laboratory to laboratory, but the main components are: A power generator responsible to transform 50 to 60 Hz voltage signal into 20 kHz ultrasonic electrical sinusoidal signal, a piezoelectric converter that transforms

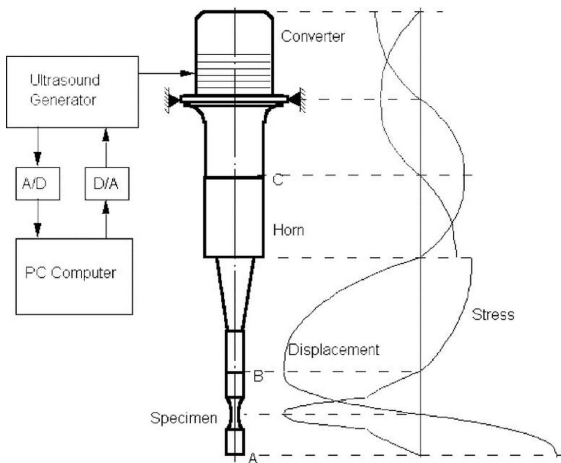


Figure 3. Schematic drawing of the displacement and stress distribution along the system with the main components of an ultrasonic fatigue machine⁷.

the electrical signal into longitudinal ultrasonic waves and vibration (mechanical loading) of the same frequency, an ultrasonic horn that amplifies the vibration coming from the piezoelectric converter in order to obtain the required strain amplitude in the middle section of the specimen (necessary to perform the tests) and a computer for data acquisition.

3.2. Specimens design

Figures 4 and 5 present the geometry and dimensions of the specimens according to Bathias book⁷. The resonance length of DIN 34CrNiMo6 specimens is 15.38 mm and for AISI 316L (AM) is 15.89 mm.

4. Results

4.1. S-N curves

Figures 6 and 7 present the plotted S-N data for both groups of specimens. As shown, all the experiments were carried out aiming for 10⁹ cycles (run out). Both materials show a tendency of higher life for lower stresses in the VHCF regime even with considerable scatter in the results. In the two situations, an equation was obtained to predict the fatigue life based on the plotted data of specimens that failed during the tests. For the DIN 34CrNiMo6 specimens, the applied stresses that caused fatigue failure are shown to be higher than expected for the VHCF regime, achieving levels almost equivalent to half of the ultimate tensile strength of the

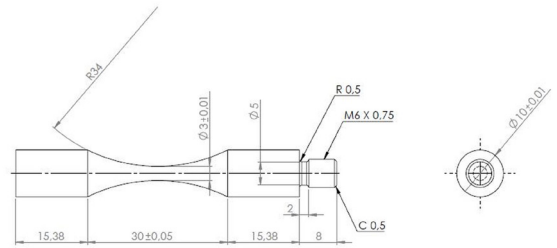


Figure 4. DIN 34CrNiMo6 specimen hourglass shape with dimension in mm.

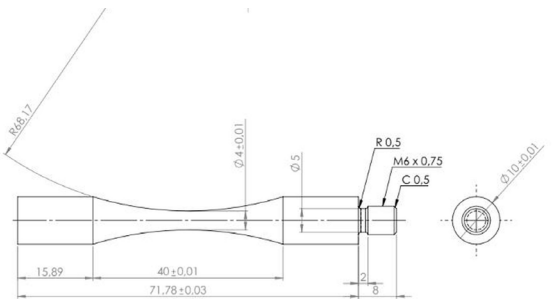


Figure 5. AISI 316L (AM) specimen hourglass shape with dimension in mm.

Table 3. L-DED process parameters.

Laser power (W)	Spot size (mm)	Laser intensity (W/mm ²)	Scanning speed (mm/min)	Feed rate (g/min)	Carrier gas flow (L/min)	Shielding gas flow (L/min)	Hatch spacing (mm)
1300	1.78	522.41	1446	30	6	40	1.223

material under study. In fact, two of the run-out specimens did not fail under the action of stress higher than 450 MPa.

The high dispersion observed in the results of AISI 316L (AM), Figure 7, is due to the number of internal defects that exist and that are not replicated in all samples. Fatigue strength for $1.0E+09$ corresponds to stress values equivalent to 35% of the ultimate tensile strength (σ_u), which is consistent with the literature (the literature mentions that fatigue strength for $1.0E+07$ cycles is equivalent to this percentage of σ_u)⁷. In addition, for the specimens that failed before $1.0E+07$, the crack initiation site was pore and surface defects. As for the specimens that failed within the VHCF regime, the non-metallic inclusions were the mandatory defect for crack nucleation.

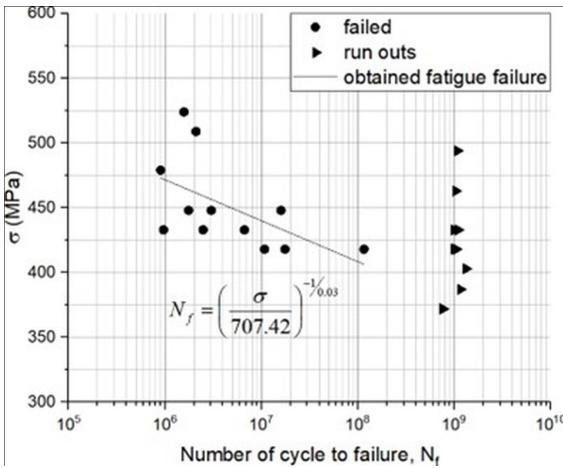


Figure 6. S-N data of DIN 34CrNiMo6 steel.

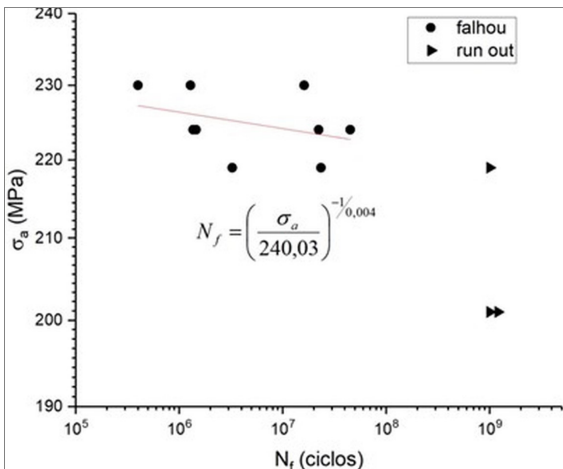


Figure 7. S-N data of AISI 316L (AM) steel.

Table 4. Specimens selected for fractographic analysis.

Specimens n°	Material	σ_a (MPa)	N_f (cycles)	CNS
1	DIN 34CrNiMo6	524	1.58E+06	Internal
2	DIN 34CrNiMo6	418	1.02E+08	Subsurface
3	AISI 316L (AM)	219	2.34E+07	Internal
4	AISI 316L (AM)	224	2.22E+07	Subsurface

4.2. FGA size and estimates

Two specimens for each material were investigated by scanning electron microscopy (SEM). Table 4 summarizes the information about the material, applied stress amplitude (σ_a), corresponding fatigue life (N_f) and the crack nucleation site (CNS) of each specimen labeled from 1 to 4.

Details of fish-eye and FGA formation are observed in Figures 8-11. It was observed that in all cases the crack nucleation sites were from non-metallic inclusions.

After investigating the fracture surface and measuring the FGA sizes with the aid of a digital image program (DIP), the measured values were compared to the estimated ones by Equations 1, 2 and 3, as shown in Figure 12.

Based on this comparison, the measured FGA size of DIN 34CrNiMo6 specimens agrees well with Liu's formula. However, for the AISI 316L (AM) specimens, the measures of FGA size presented a greater agreement with the results estimated by Yang's model. Although the result estimated by Yang's equation presented a large variation compared to the FGA size measured in specimen 3, considering the two situations it was the most suitable. The difference between these models is related to the mechanical property used as a calculation parameter for estimating the FGA size. While the Yang model considers the yield stress as the mandatory parameter, the others consider Vickers hardness. Considering these two mechanical properties, it is assumed that the Yang Model presented better results due to the lower dispersion between the values obtained for the yield stress. This is more noticeable in Figure 13, where is shown the percentage difference (error index) between measured and calculated values of FGA size for all specimens in question. The results obtained by Murakami's equation presented the worst agreement with the measured values for the four situations.

It was also verified that the measured FGA size ($\approx 700 \mu\text{m}$) in specimen n°3 by DIP for subsurface fish-eye agrees well with the literature²⁶.

The fish-eye size was also measured and compared with FGA size in function of the stress amplitude, as shown in Figure 14. It was noticed that FGA and fish-eye sizes rise with the increasing stress amplitude for AISI 316L (AM) specimens. However, for DIN 34CrNiMo6 specimens the opposite happens. FGA and fish-eye sizes decrease with the increase of stress amplitude.

Moreover, the maximum stress intensity factor (SIF) at FGA and fish-eye boundaries were calculated using the Equation 4^{27,28} to identify the threshold for internal short crack propagation and the threshold for circular crack propagation. Table 5 presents the ΔK_{FGA} and $\Delta K_{fish-eye}$ values for all situations.

$$\Delta K_{FGA \text{ or } fish-eye} = 2K_{max-FGA \text{ or } fish-eye} = \frac{4}{\pi} \sigma_a \sqrt{\pi * \sqrt{area}} \quad (4)$$

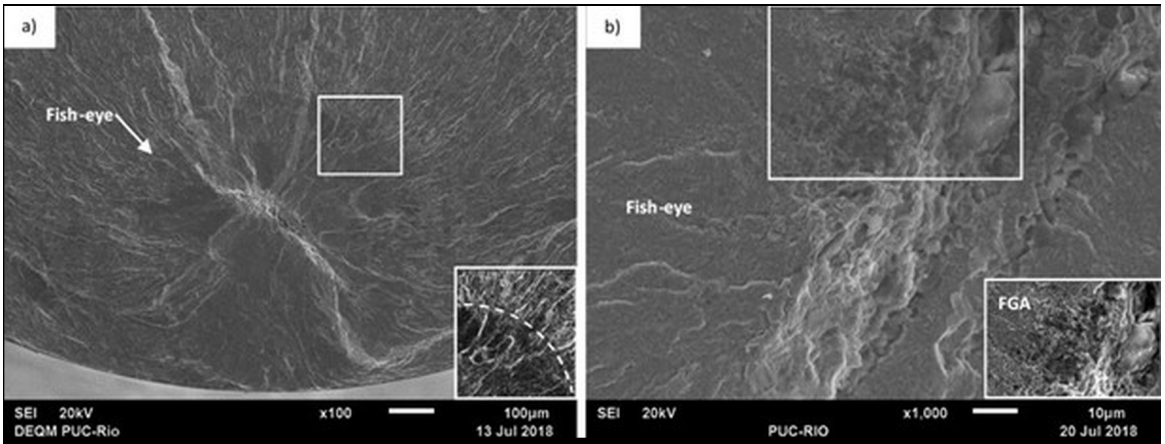


Figure 8. SEM of fracture surface of Specimen n°1: a) Fish-eye formation and its border in the magnification; b) Magnification inside the Fish-eye and FGA regions^{20,21}.

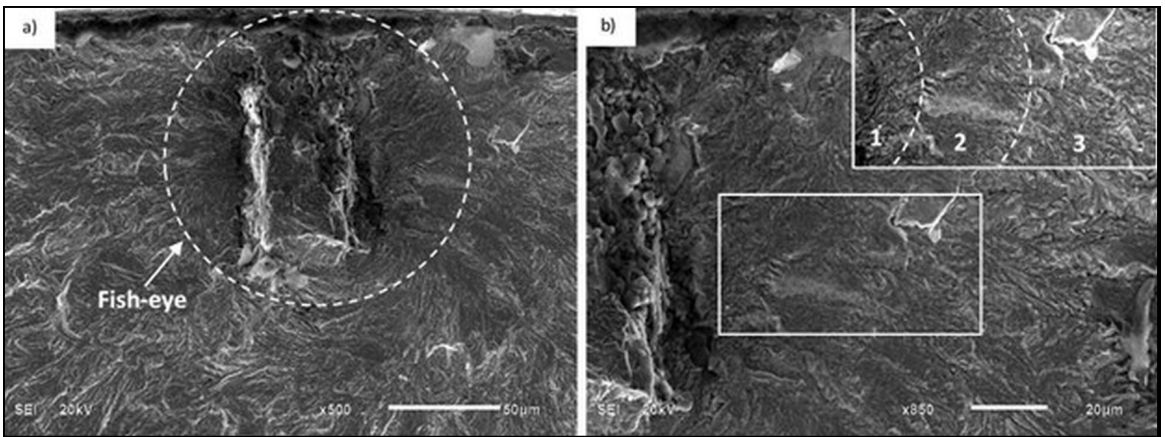


Figure 9. SEM of fracture surface of Specimens n° 2. a) Fish-eye formation; b) Magnification of the right side region (detailed: 1-fine grain, 2-fish-eye, 3-outside the fish-eye)^{20,21}.

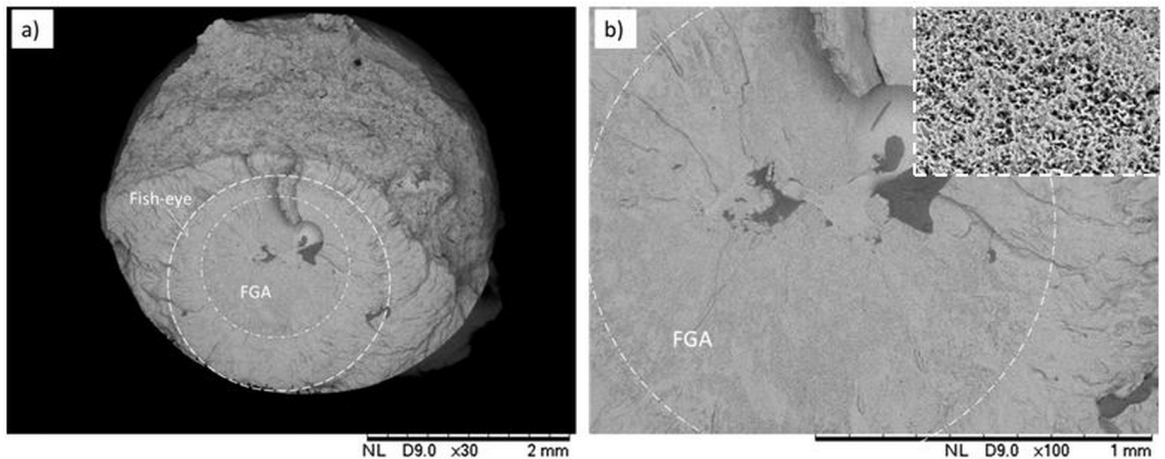


Figure 10. SEM of fracture surface of Specimen n° 3: a) Fish-eye formation; b) Magnification of FGA area with fine grain detailed.

Based on calculated values of ΔK_{FGA} and $\Delta K_{fish-eye}$, it is noticeable that for DIN 34CrNiMo6 specimens the $\Delta K_{fish-eye}$ is higher (around 3x) than ΔK_{FGA} (internal crack nucleation).

For AISI 316L (AM) specimens these values differ briefly. This is explained because the crack propagation to form the FGA consumes a large part of the area inside the fish-eye

Table 5. Maximum SIF of VHCF tested specimens.

Specimens n°	Material	σ_a (MPa)	$\Delta K_{FGA}(\text{MPa} \sqrt{m})$	$\Delta K_{fish-eye}(\text{MPa} \sqrt{m})$
1	DIN 34CrNiMo6	524	4.22	15.47
2	DIN 34CrNiMo6	418	5.67	17.74
3	AISI 316L (AM)	219	6.83	7.95
4	AISI 316L (AM)	224	8.86	11.02

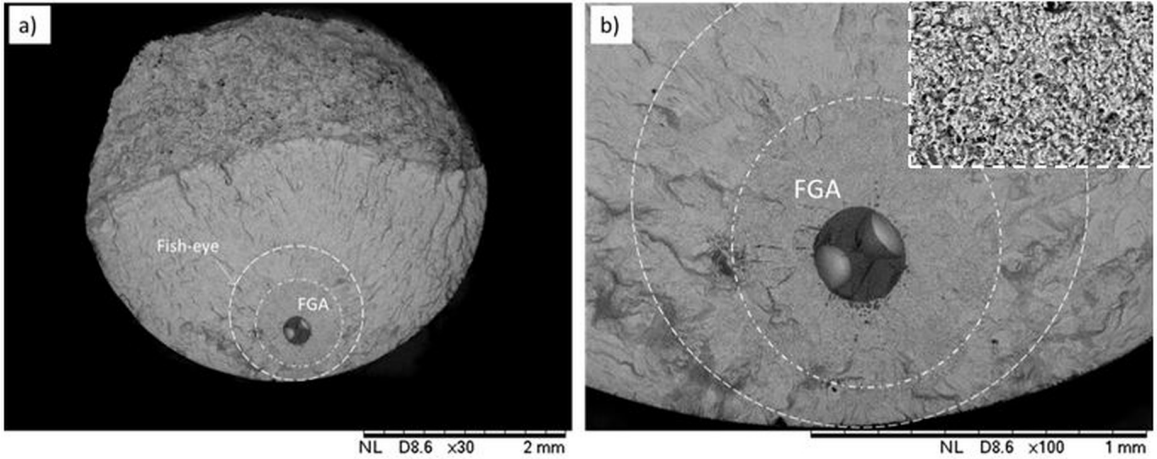


Figure 11. SEM of fracture surface of Specimen n° 4: a) Fish-eye and FGA formations; b) Magnification of FGA area.

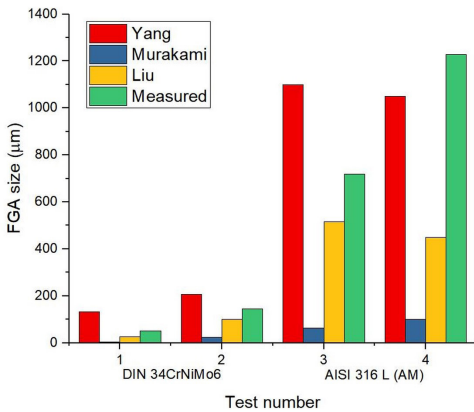


Figure 12. Comparison between measured and estimated FGA size.

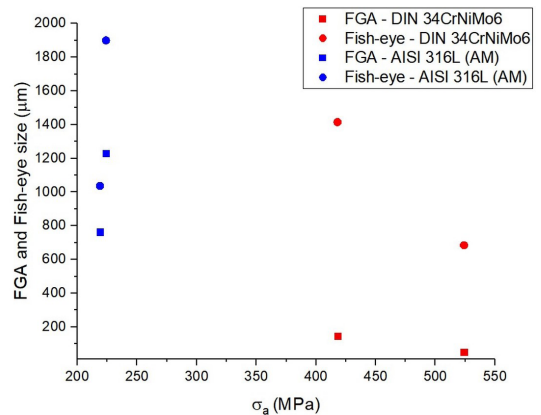


Figure 14. Fish-eye and FGA size x stress amplitude.

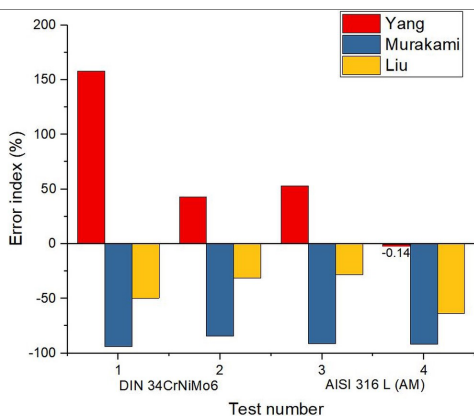


Figure 13. Error index for each model and steel.

region, which is in line with the literature²⁶ for the same material and build direction of the AM process.

5. Conclusions

The following conclusions can be drawn:

- The crack nucleation in the VHCF regime for AM materials follows the same behavior and the cracks tend to start internally;
- The FGA size measured on the fracture surface agrees well with the results estimated by Liu et al. for DIN 34CrNiMo6 specimens and the relationship proposed by Yang et al. was better suitable for AISI 316L (AM) measures;
- Murakami’s expression underestimated the FGA size measures for both materials;

- For the DIN 34CrNiMo6 steel, the mean values of ΔK_{FGA} and $\Delta K_{fish-eye}$ were found around $4 \text{ MPa}\sqrt{m}$ and $16 \text{ MPa}\sqrt{m}$. For AISI 316L (AM) steel, $8 \text{ MPa}\sqrt{m}$ for ΔK_{FGA} and $\Delta K_{fish-eye}$ equals to $9 \text{ MPa}\sqrt{m}$, were obtained respectively.

6. Acknowledgments

This work was developed within the scope of the Research and Technological Development of the Brazilian Electric Energy Sector Program regulated by ANEEL, with the support of the Eneva Companies - Pecém II Energy Generation S.A., Itaqui Energy Generation S.A. and Parnaíba I, II and III Energy Generation S.A. and in partnership with SENAI Institute of Innovation in Manufacturing Systems and Laser Processing, FIESC-SENAI/SC.

The authors would like to thank FAPERJ (Fundação de amparo à pesquisa do estado do Rio de Janeiro) for the financial support through project n.2021/00674-8.

7. References

- Honarvar F, Varvani-Farahani A. A review of ultrasonic testing applications in additive manufacturing: defect evaluation, material characterization, and process control. *Ultrasonics*. 2020;108:106227.
- European Powder Metallurgy Association – EPMA. Introduction to additive manufacturing technology: a guide for designers and engineers. Shrewsbury, UK: EPMA; 2015.
- Miedzinski M. Materials for additive manufacturing by direct energy deposition – identification of materials properties that can have an influence on the building process or the resulting component properties. Göteborg: Chalmers University of Technology; 2017.
- Gibson I, Rosen DR, Stucker B. Additive manufacturing technologies – rapid prototyping to direct digital manufacturing. New York: Springer, 2010.
- Mahamood RM. Laser metal deposition process of metals, alloys, and composite materials. Manchester: Springer, 2018.
- Sabbori A, Aversa A, Marchese G, Biamino S, Lombardi M, Fino P. Microstructure and mechanical properties of AISI 316L produced by direct energy deposition-based additive manufacturing: a review. *Appl Sci (Basel)*. 2020;10(9):3310.
- Bathias C, Paris PC. Gigacycle fatigue of mechanical practice. New York: Marcel Dekker Inc.; 2005.
- Pyttel B, Schwerdt D, Berger C. Very high cycle fatigue - is there a fatigue limit? *Int J Fatigue*. 2011;33:49-58.
- Bathias C, Drouillac L, Le François P. How and why the fatigue SN curve does not approach a horizontal asymptote. *Int J Fatigue*. 2001;23:S143-51.
- Kazymyrovych V. Very high cycle fatigue of engineering materials - a literature review. Karlstad: Karlstad University Studies; 2009.
- Kazymyrovych V. Very high cycle fatigue of tool steel. Karlstad: Karlstad University Studies; 2010.
- Marines I, Bin X, Bathias C. An understanding of very high cycle fatigue of metals. *Int J Fatigue*. 2003;25:1101-7.
- Sakai T. Review and prospects for current studies on very high cycle of metallic materials for machine structural use. *J Solid Mech Mater Eng*. 2009;3:425-39.
- Murakami Y. Metal fatigue: effects of small defects and nonmetallic inclusions. USA: Elsevier; 2002.
- Murakami Y, Matsunaga H. The effect of hydrogen on fatigue properties of steels used for fuel cell system. *Int J Fatigue*. 2006;28(11):1509-20.
- Liu YB, Li SX, Li YD, Yang ZG. Factors influencing the GBF size of high strength steels in the very high cycle fatigue regime. *Mater Sci Eng*. 2011;358:935-42.
- Yang ZG. Estimation of the size of GBF area on fracture surface for high strength steels in very high cycle fatigue regime. *Int J Fatigue*. 2008;30:1016-23.
- Li YD, Zhang L-L, Fei Y-H, Liu X-Y, Li M-X. On the formation mechanisms of fine granular area (FGA) on the fracture surface for high strength steels in the VHCF regime. *Int J Fatigue*. 2016;82:402-10.
- Pereira MV, Teixeira MC, Darwish FA. Correlation between fractographic aspects and stress intensity factor in very high cycle fatigue. *Procedia Struct Integr*. 2019;17:105-14.
- Teixeira MC, Costa PR, Pereira MV, Freitas M, Reis L. Fractographic features of VHCF tested specimens and their relation to stress intensity factor. *J Mater Res Technol*. 2022. In press.
- Teixeira MC. Comportamento do aço DIN 34CrNiMo6 em fadiga de altíssimo ciclo [dissertation]. Rio de Janeiro: PUC-Rio; 2018.
- Thiesen A Jr. Selection of processing parameters for the laser directed energy deposition process applied to additive manufacturing: a methodological proposal [dissertation]. Joinville: UFSC; 2021.
- ASTM: American Society for Testing and Materials. ASTM A370: Standard Test Methods and Definitions for Mechanical Testing of Steel Products. West Conshohocken: ASTM; 2022.
- Andrade MF. Avaliação da super longa vida em fadiga do aço inoxidável AISI 316L processado por manufatura aditiva L-DED [dissertation]. Rio de Janeiro: PUC-Rio; 2022.
- Andrade MF, Pereira MV, Teixeira MC, Junior AT, Gutjar J. Fatigue life assessment in the very high cycle regime of AISI 316L stainless steel processed by L-DED additive manufacturing. *Procedia Struct Integr*. 2022;42:1008-16.
- Voloskov B, Evlashin S, Dagesyan S, Abaimov S, Akhatov I, Sergeichev I. Very high cycle fatigue behavior of additively manufactured 316L stainless steel. *Materials (Basel, Switzerland)*. 2020;13(15):3293.
- Marines-Garcia I, Paris PC, Tada H, Bathias C, Lados D. Fatigue assessment using an integrated threshold curve method - applications. *Eng Fract Mech*. 2008;75:1657-65.
- Li W, Sun Z, Deng H, Zhang Z, Sakai T. Interior crack initiation and growth behaviors and life prediction of carburized gear steel under high cycle fatigue and very high cycle fatigue. *J Mater Res*. 2015;30(14):2247-57.